

Article

Performance Evaluation of LIDAR and SODAR Wind Profilers on the Brazilian Equatorial Margin

Audalio R. Torres Junior ^{1,2,*} , Natália P. Saraiva ² , Arcilan T. Assireu ³ , Francisco L. A. Neto ⁴ ,
Felipe M. Pimenta ⁵ , Ramon M. de Freitas ⁶ , Osvaldo R. Saavedra ² , Clóvis B. M. Oliveira ² ,
Denivaldo C. P. Lopes ² , Shigeaki L. de Lima ² , Rafael B. S. Veras ²  and Denisson Q. Oliveira ² 

- ¹ Programa de Pós-Graduação em Oceanografia, Universidade Federal do Maranhão, Av. dos Portugueses s/n, São Luís 65080-040, MA, Brazil
 - ² Instituto de Energia Elétrica, Universidade Federal do Maranhão, Av. dos Portugueses s/n, São Luís 65080-040, MA, Brazil
 - ³ Instituto de Recursos Naturais, Universidade Federal de Itajubá, Av. BPS 1303, Pinheirinho, Itajubá 37500-903, MG, Brazil
 - ⁴ Laboratório de Meteorologia Aplicada, Universidade Federal do Rio de Janeiro, Rio de Janeiro 21941-916, RJ, Brazil
 - ⁵ Centro de Ciências Físicas e Matemáticas, Programa de Pós-Graduação em Oceanografia, Campus Trindade, Universidade Federal de Santa Catarina, Florianópolis 88040-900, SC, Brazil
 - ⁶ Camargo Schubert Wind Engineering, Rua Juvenal Galeno, 55-Jardim Social, Curitiba 82520-030, PR, Brazil
- * Correspondence: audalio.torres@gmail.com



Citation: Junior Torres, A.R.; Saraiva, N.P.; Assireu, A.T.; Neto, F.L.A.; Pimenta, F.M.; de Freitas, R.M.; Saavedra, O.R.; Oliveira, C.B.M.; Lopes, D.C.P.; de Lima, S.L.; et al. Performance Evaluation of LIDAR and SODAR Wind Profilers on the Brazilian Equatorial Margin. *Sustainability* **2022**, *14*, 14654. <https://doi.org/10.3390/su142114654>

Academic Editor: Firoz Alam

Received: 3 October 2022

Accepted: 3 November 2022

Published: 7 November 2022

Publisher's Note: MDPI stays neutral with regard to jurisdictional claims in published maps and institutional affiliations.



Copyright: © 2022 by the authors. Licensee MDPI, Basel, Switzerland. This article is an open access article distributed under the terms and conditions of the Creative Commons Attribution (CC BY) license (<https://creativecommons.org/licenses/by/4.0/>).

Abstract: This article seeks to compare the performance of a LIDAR Windcube V2, manufactured by Leosphere, with that of a SODAR MFAS, manufactured by Scintec, in evaluating wind speed at different altitudes. The data from these two sensors were collected at three locations on the Brazilian equatorial margin in the state of Maranhão. The comparison of these sensors aims at their simultaneous use at different points. The horizontal velocity components, by altitude, showed Pearson correlation values above 0.9 and values for the vertical velocity component between 0.7 and 0.85. As for the sampling efficiency, the LIDAR had a performance slightly higher than that of SODAR, especially at the point closest to the coast. In general, both sensors showed similar values, despite the differences in sampling methods. The results showed that the joint performance of these sensors had good correlation, being reliable for application in estimating wind potential for power generation in coastal areas of the equatorial region.

Keywords: wind potential; equatorial margin; LIDAR; SODAR

1. Introduction

A project is in progress in the state of Maranhão, Brazil to map the potential for electricity generation by using wind as one of the primary sources. Its main objective is to evaluate wind and solar resources using in situ observational data, remote sensing data, and atmospheric reanalysis [1]. To obtain information on wind energy at low levels, two wind estimation systems were acquired based on remote sensing techniques: Light Detection and Ranging (LIDAR) which uses electromagnetic waves [2], and Sound Detection and Ranging (SODAR) [3], which probes the atmosphere with sound waves [4,5]. The comparison of these sensors is significant due to their employment in different locations within the project's study area. Its estimated or "measured" parameters describe the air movement from the information of the wind's direction, orientation, and intensity, as well as the statistics produced based on the sampling techniques of each sensor. Obtaining these parameters basically depends on the physics of the propagation of electromagnetic and acoustic waves [2,3,6–13].

Renewable energies, especially wind, are playing a leading role in the process of decarbonization of the electric matrix, as well as in the green hydrogen generation chain.

The equatorial margin of the north-northeast region of Brazil presents advantageous natural conditions for wind energy production both on shore and off shore. Key components to this very favorable scenario are the trade winds that are characteristic of the equatorial region and occur regularly throughout all months of the year.

As a consequence, many initiatives that aim to deepen the knowledge of and better characterize this region are being carried out, while others are on course. In this way, new technologies for measuring wind potential have evolved significantly in recent years, where the LIDAR and SODAR profiling devices stand out. These devices have gained ground in measurement campaigns in wind farms worldwide, and some papers reported on their performance individually and comparatively [3,9,11,14,15]. However, no experimental validation research was performed under typical equatorial conditions (e.g., with high temperatures, humidity gradients, and peculiar relief and vegetation).

In this paper, we present an experimental study on the comparative performance of these two types of profilers at three locations on the Brazilian equatorial margin in the state of Maranhão. This research is part of the Evaluation of the micrometeorological effects in different temporal and spatial scales in the planning and operation of wind farms and photovoltaics (EOSOLAR) project, which made the field activities for this work possible. Here, we briefly describe these locations, the climatology of the region, some characteristics of the sensors, and their sampling methodology. We present a methodology to compare these instruments and discuss aspects associated with the atmospheric boundary layer in the transition of the ocean to the continent.

2. Measurement Campaigns: Sites and Procedures

The measurements took place at three sites, all in the state of Maranhão. The first was on the campus of the Federal University of Maranhão (UFMA, São Luís, Brazil) in the city of São Luís, an urban and insular region (UFMA point in Figure 1). The other two measurement campaigns were carried out in the town of Paulino Neves, located about 190 km east of São Luís, represented in Figure 1 by the points marked as *Praia* and *Giba*.

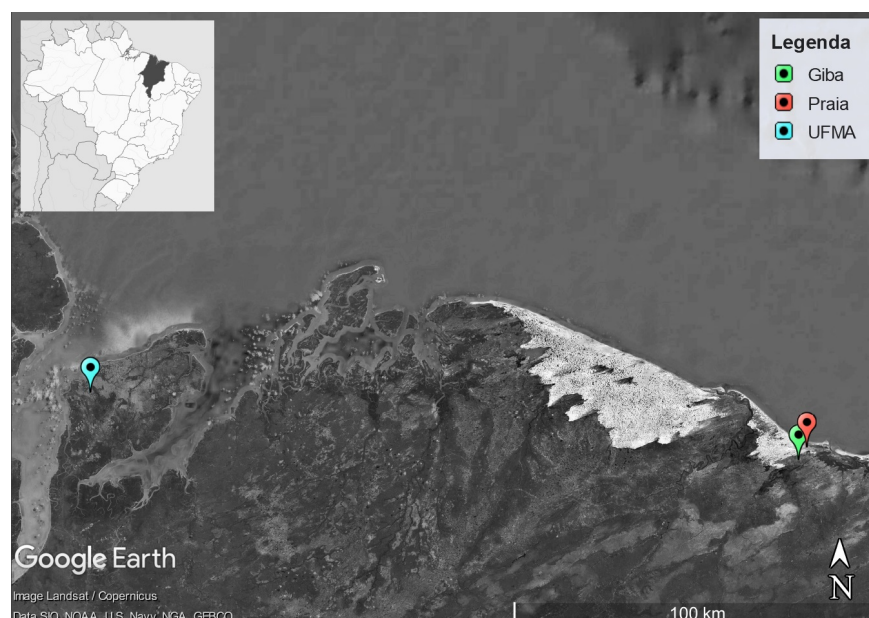


Figure 1. Eastern coast of Maranhão state in Brazil, showing the positions of the UFMA (at UFMA’s Electric Energy Institute in the city of São Luís), *Praia*, and *Giba* (both in the city of Paulino Neves) campaigns.

During the first campaign, the devices were installed at UFMA’s Electric Energy Institute (IEE) at longitude 44.307° W and latitude 2.560° S. For safety, the LIDAR was installed on the roof of the IEE, about 3.5 m high, while the SODAR was maintained at

ground level (Figure 2). This campaign refers to the longest comparison time between the devices, comprising 20 days in duration from 7 to 26 August 2021 (Table 1).

Table 1. Periods, total days, locations of the instruments, and distances from the coastline during the measurement campaigns.

Campaigns	Period	No. of Days	Location	Sea Distance
UFMA ¹	7 August 2021, 12:00:01 a.m. to 26 August 2021, 11:50:01 p.m.	20	IEE-UFMA (2.560° S, 44.307° W)	4–8 km
Praia	9 November 2021, 2:10:01 p.m. to 10 November 2021, 1:50:01 p.m.	20	Near the beach (2.694° S, 42.555° W)	1.3 km
Giba	10 November 2021, 5:20:01 p.m. to 12 Novemebr 2021, 10:40:01 a.m.	01	Mr. Gilberto Porto's farm (2.725° S, 42.575° W)	5.6 km

¹ In this campaign, the LIDAR was at a 3.5-m height.

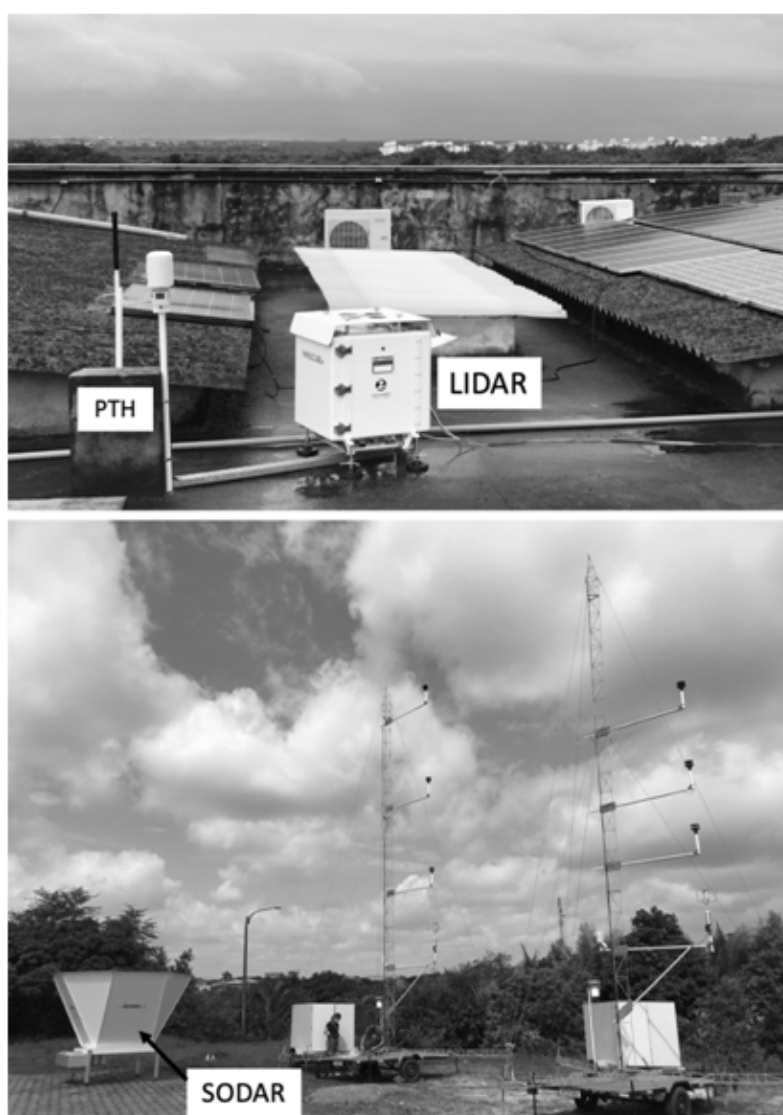


Figure 2. UFMA campaign (IEE-UFMA, 44.307° W, 2.560° S). (**upper**) LIDAR wind profiler installed 3.5 m from the ground on the roof. (**bottom**) SODAR installed at ground level in the parking lot.

The second campaign was conducted near the beach at the point called *Praia*, located at longitude 42.555° W and latitude 2.694° S, between 9 and 10 November 2021 (Table 1). The distance between the sea and this point was estimated to be 1300 m by Google satellite

imagery. However, the beach has a low slope and is vulnerable to flooding during astronomical tides. Macro-tidal flooding occurs in this region, which causes high variations in the amplitude of the sea level [16] (Figure 3).

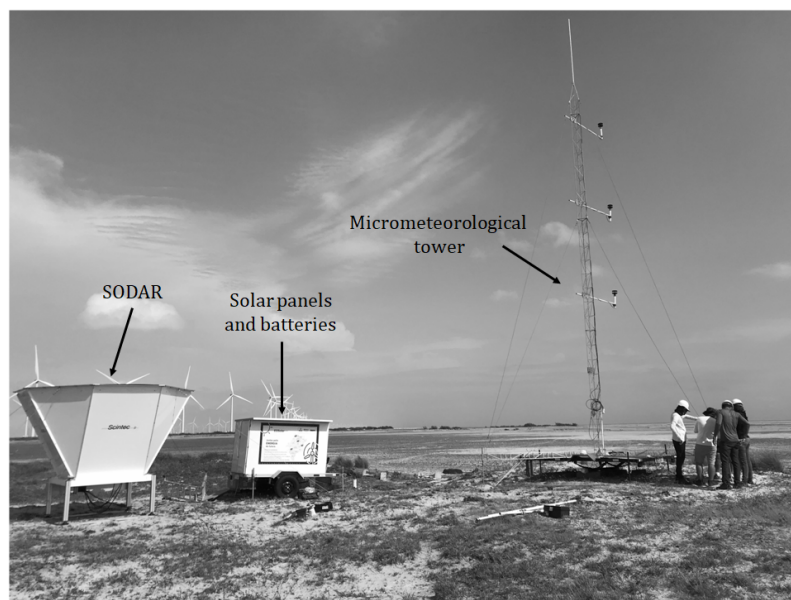


Figure 3. Praia campaign (42.555° W, 2.694° S), showing the SODAR and micrometeorological tower set-up. This point is located about 1300 m from the beach line and windward of the wind turbines of the Delta wind farm in Paulino Neves.

The last campaign was carried out at a point further from the coast on Mr. Gilberto Porto's farm, called *Giba* in this study, at longitude 42.575° W and latitude 2.725° S. It is a region with low dunes and a little slope, having low vegetation and bushes (Figure 4). At this site, the measurements were conducted between 10 and 12 November 2021.

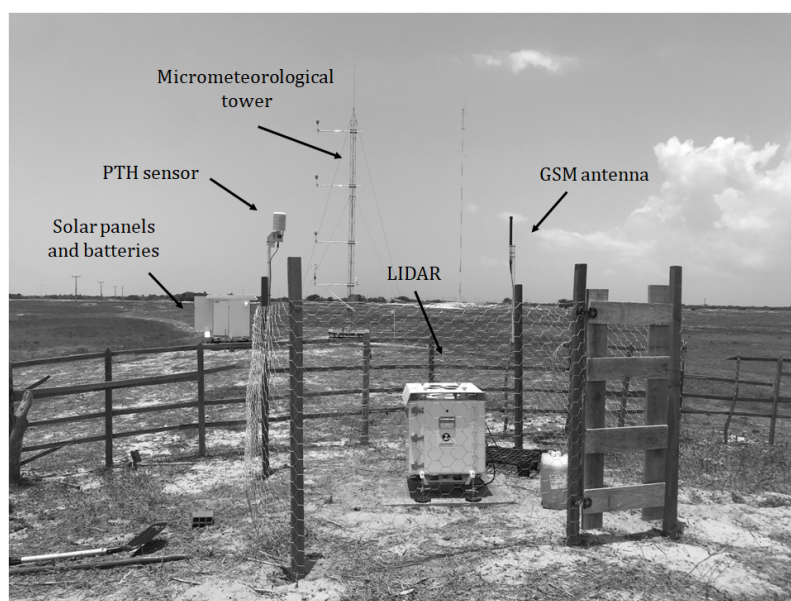


Figure 4. Giba campaign (-42.575° W, -2.725° S), showing the LIDAR installation. This point is located about 3.4 km from the Praia point in a region with low vegetation and bushes.

3. Regional Climatology

The local weather patterns, and thus the generation of electricity based on the transformation of both the energy of the air motion and solar radiation, depend on the climatology

in the region of study. The EOSOLAR project [1] will collect data over the course of a year, allowing us to understand the variability in wind and solar sources at different time and space scales. In the study region, climatology is governed mainly by local aspects dependent on topography, vegetation, proximity to the ocean, and latitude, which define the solar irradiation that reaches the ground. However, some large-scale spatial and temporal agents influence the local climate. Among them, we can mention the following:

- With intervals between 2 and 7 years, the atmospheric teleconnections El Niño and La Niña have impacts on global atmospheric circulation, with well-defined effects on various “climatic” patterns in Brazil, such as precipitation and wind circulation in the northeast [17–30];
- The intertropical convergence zone (ITCZ) and its seasonal periods define changes in cloud patterns, precipitation, wind direction, and intensity in the region [31–38];
- The seasonally periodic South American monsoon also influences local weather patterns [39–45];
- The effects of Madden–Julian oscillations with a periodicity between 40 and 50 days [46–55];
- The easterly waves, with a typical periodicity of 4 days [37,56–61];
- The sea and land breeze with daily cycles [62–71].

4. LIDAR and SODAR Wind Profilers

Wind profilers use different forms of energy to detect targets in air parcels and estimate motion from their transport with the Doppler-Fizeau effect [72]. The operating wavelength of our LIDAR (Windcube V2, manufactured by Leosphere) was 1543 nm [73], and that of our SODAR (MFAS, manufactured by Scintec) was to the order of 0.12–0.2 m [74] (i.e., seven orders of magnitude greater).

As for the targets of the sensors, SODAR detects deformations in the flow or inhomogeneities of the air density field, while LIDAR detects particles (aerosols) transported in the atmosphere. In both sensors, the return signal or backscatter of the targets is analyzed, and the radial velocity, also called the line of sight velocity, is estimated. The measurement of the radial velocity in different directions makes it possible to compose the wind velocity vector at different vertical levels.

The beam geometry and sampling windows of the return signals from these sensors are different. LIDAR emits four oblique beams in the north, south, east, and west directions at an angle of 28° from vertical and a vertical beam [75]. SODAR emits nine acoustic beams, with the main beam emitted vertically at 0° and eight beams in pairs of complementary pulses in opposite directions (from 29° to -22°) in the north, east, south, and west directions (Figure 5).

From temporal averages of the samples performed in the detected horizontal layers, the wind characteristics are estimated differently between both sensors. The frequencies of electromagnetic waves (LIDAR) and sound waves (SODAR) detect different structures (targets), so naturally, there will be differences in sensor performance depending on the environmental conditions. In this paper, the difference between the performances of these wind profilers will be shown.

Both devices were configured for measurements with intervals of 10 m from 50 to 200 m in height and 20 m from 200 to 280 m in height (Table 2). However, we emphasize that each device’s horizontal slab length was different. While the horizontal slab length of the SODAR was 10 m, that of the LIDAR was 20 m (Figure 6).

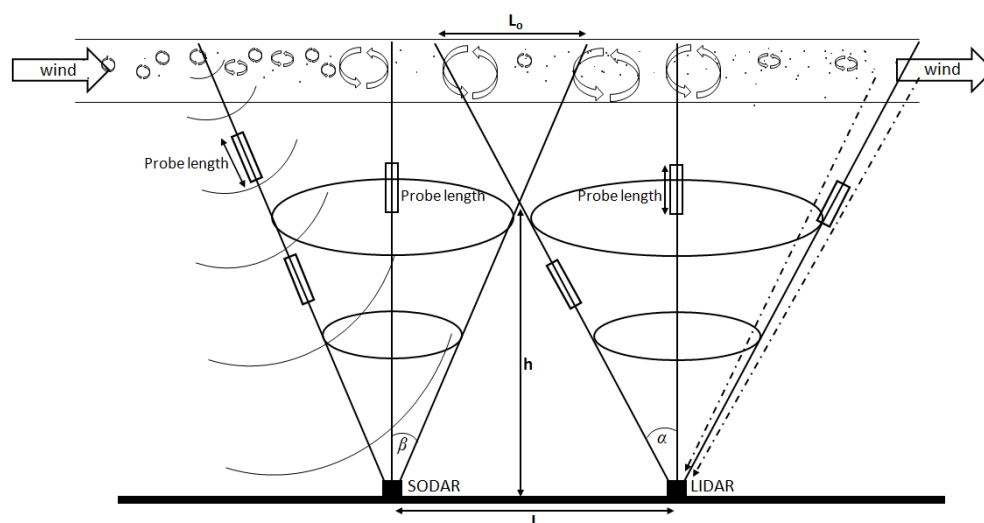


Figure 5. Geometries of the beams emitted by LIDAR and SODAR for the *UFMA* campaign. LIDAR was positioned 3.5 m above the surface. α and β are the angles concerning the vertical beam emitted by LIDAR (28°) and SODAR (from 29° to -22°), respectively.

Table 2. Height of measurements (m), linear overlap (m), sector length sampled by LIDAR and SODAR added together, and overlapping linear percentage sampled relative to total length (LIDAR + SODAR).

Height (m)	Linear Overlap (m)	LIDAR + SODAR	Overlap or Total
50	38	108	35.2%
60	49	130	37.7%
70	60	152	39.5%
80	71	174	40.8%
90	82	195	42.1%
100	93	217	42.9%
110	104	239	43.5%
120	115	261	44.1%
130	126	282	44.7%
140	137	304	45.1%
150	148	326	45.4%
160	159	347	45.8%
170	170	369	46.1%
180	181	391	46.3%
190	192	413	46.5%
200	203	434	46.8%
220	226	478	47.3%
240	248	521	47.6%
260	270	565	47.8%
280	292	608	48.0%

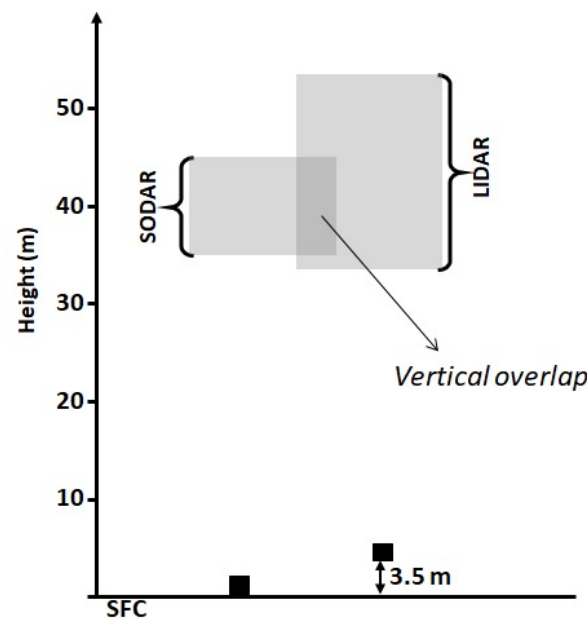


Figure 6. Schematic of the vertical overlap of the sample volume length at the 40-m measurement height for LIDAR and SODAR during the UFMA campaign (Figure 1 and Table 1). SFC indicates surface or ground level. Note that the LIDAR was at a 3.5-m height.

Therefore, the vertical overlap sampled was at least 10 m between the instruments. The calculation of the horizontal overlap will be demonstrated in the next section. Table 2 lists the coincident horizontal layers sampled by LIDAR and SODAR.

5. Methodology

To compare measurements of the parameters associated with wind speed obtained from SODAR and LIDAR, observing the basic principles that each technology uses in its estimates is necessary. After analyzing the differences between the principles of estimation of the parameters obtained by each remote sensor, we define that the methodology presented by Pearson's correlation is the most appropriate method for performing this comparison.

The Pearson's correlation coefficients (PCCs) [76] were calculated among the variables obtained by the LIDAR and SODAR sensors for the zonal (east-west), meridional (north-south), and vertical components by the horizontal layers:

$$PCC_{X,Y} = \frac{Cov(X,Y)}{\sigma_x \sigma_y}, \quad (1)$$

where x and y are the variables to be correlated, Cov is the covariance between x and y , and σ_x and σ_y are the standard deviations of x and y , respectively. The covariance is calculated by

$$Cov(x,y) = \frac{1}{n} \left[\sum_{i=1}^n x_i y_i - \frac{1}{n} \left(\sum_{i=1}^n x_i \right) \left(\sum_{i=1}^n y_i \right) \right], \quad (2)$$

where n is the number of paired samples. The time averages were also calculated for each height:

$$\mu_\zeta = \frac{1}{n\tau} \sum_{\tau=1}^{n\tau} \varphi_\zeta^\tau, \quad (3)$$

where φ is the variable, ζ is the height, and τ is the time.

Note that this methodology is usual for comparison between meteorological data estimation platforms and has been widely used in applications of remote sensing of air movement [2,7–9,13,77,78].

The calculations to estimate the linear overlap, generated through the horizontal layers sampled by both sensors, were based on the geometry shown in Figure 7, where we knew the following:

- L_{s1} is the distance between the LIDAR and the SODAR;
- α is the scanning cone angle of the LIDAR;
- β is the angle of the scanning cone of SODAR;
- δ is the height of the LIDAR.

As already mentioned, the LIDAR was at a height of $\delta = 3.5$ m during the *UFMA* campaign but $\delta = 0$ at the other points (*Praia* and *Giba*). In the *UFMA* campaign, the horizontal distance between the sensors was 15 m, and in the other two, was 8 m.

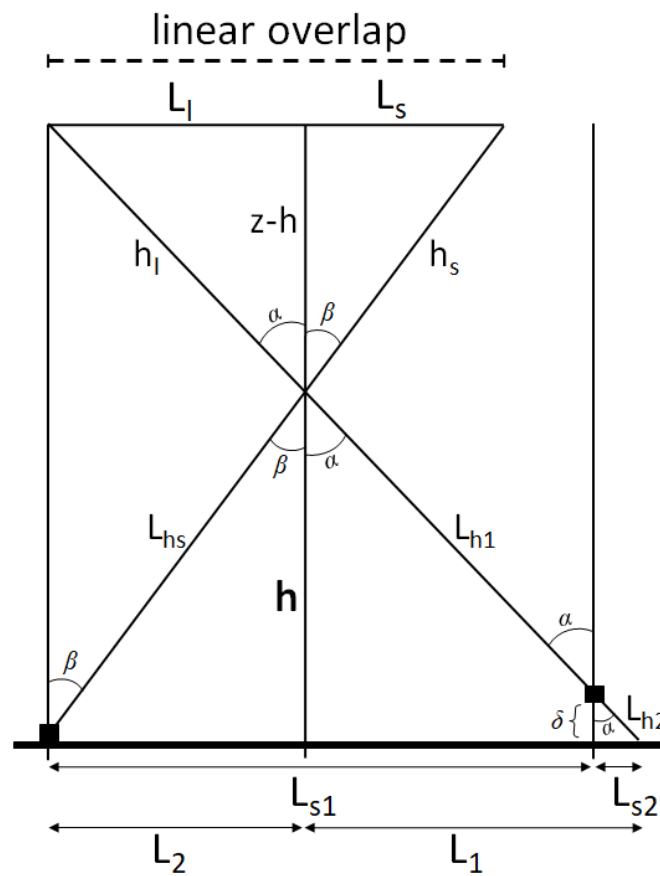


Figure 7. The geometry used to estimate the superposition region of the horizontal layers sampled by LIDAR and SODAR.

From the geometric relationships observed in Figure 7, we obtained

$$\frac{\alpha}{\beta} = \frac{L_1}{L_2} \Rightarrow L_2 = L_1 \frac{\beta}{\alpha}, \text{ and} \tag{4}$$

$$L_1 + L_2 = L_{s1} + L_{s2}. \tag{5}$$

By substituting Equation (4) into Equation (5), we obtain

$$L_1 + L_{s1} \frac{\beta}{\alpha} = L_{s1} + L_{s2} \Rightarrow L_1 = \frac{L_{s1} + L_{s2}}{\left(1 + \frac{\beta}{\alpha}\right)}. \tag{6}$$

From the relations obtained by the triangle formed below the LIDAR (Figure 7), we find L_{s2} :

$$L_{s2} = \sqrt{L_{h2}^2 - \delta^2}, \quad \text{knowing that } L_{h2} = \frac{\delta}{\cos(\alpha)}, \quad (7)$$

$$\text{we have } L_{h2} = \sqrt{\left(\frac{\delta}{\cos(\alpha)}\right)^2 - \delta^2}.$$

By substituting L_{s2} from Equation (7) into Equation (6), we find the value of L_1 , and thus we find the value of L_2 by substituting L_1 into Equation (4).

Considering $L_{hl} = L_{h1} + L_{h2}$, we have

$$L_{hl}\sin(\alpha) = L_1 \Rightarrow L_{hl} = \frac{L_1}{\sin(\alpha)}, \quad \text{and} \quad (8)$$

$$L_{hs}\sin(\beta) = L_2 \Rightarrow L_{hs} = \frac{L_2}{\sin(\beta)}.$$

Now, the height h can be calculated where the linear overlapping of the two sensors started:

$$L_{hl}^2 = L_1^2 + h^2 \Rightarrow h = \sqrt{L_{hl}^2 - L_1^2}. \quad (9)$$

The overlap is estimated using

$$h_l = \frac{z - h}{\cos(\alpha)}, \quad \text{and} \quad (10)$$

$$h_s = \frac{z - h}{\cos(\beta)}.$$

Thus, for both sensors, the linear overlap is given by the sum of the following two terms:

$$2(L_{hl} + h_l)\sin(\alpha) \quad \text{for LIDAR, and} \quad (11)$$

$$2(L_{hs} + h_s)\sin(\beta) \quad \text{for SODAR.}$$

A simple calculation shows that the two sensors would sample, common to both sensors, in a region of the horizontal air layer to the order of 38 m at about 50 m in height, while the linear sum of the sector sampled by both was 108 m. Table 2 lists the extent of the matching horizontal layers sampled by LIDAR and SODAR for all the measurement heights. The percentage of linear overlap started at 35.2% at 50 m and increased to 48% at 280 m.

For the evaluation of this comparison's results, the differences concerning the layers of the atmosphere (horizontal slab length) sampled by the two sensors had to be considered. The horizontal slab length of the SODAR was 10 m, while for the LIDAR, it was 20 m, and considering the fact that the LIDAR was 3.5 m high in the *UFMA* campaign, the results in a part of the horizontal slab length were not coincident between the sensors and out of the vertical overlap, as illustrated in Figure 6.

The performance of the sensors was estimated based on the lack of information in each sample cell by layer (space), and missing values were not computed in the calculations.

6. Results and Discussions

Both LIDAR and SODAR perform a discard of the captured information through the quality control required by their systems. As a result, its performance can be impaired, presenting failures to obtain data. The comparative analysis indicated high performance by the LIDAR at *UFMA*, with a loss of information to the order of 1%. However, the SODAR showed a loss of sampling efficiency from 1% to 25%, declining more above 170 m (*UFMA* in Figure 8).

In the *Praia* campaign, the LIDAR performed well, with only a 4% loss of information. However, the SODAR had poor performance above 100 m in height. At higher heights, the SODAR's performance decreased significantly, losing about 68% of the information at 260 m in height (*Praia* in Figure 8).

The best performance of the comparison between the sensors occurred in the *Giba* campaign (*Giba* in Figure 8). The LIDAR showed a 2% loss at all heights, while the SODAR had no losses until 170 m in height. At heights higher than this, the SODAR had small performance losses, reaching 12% at 260 m.

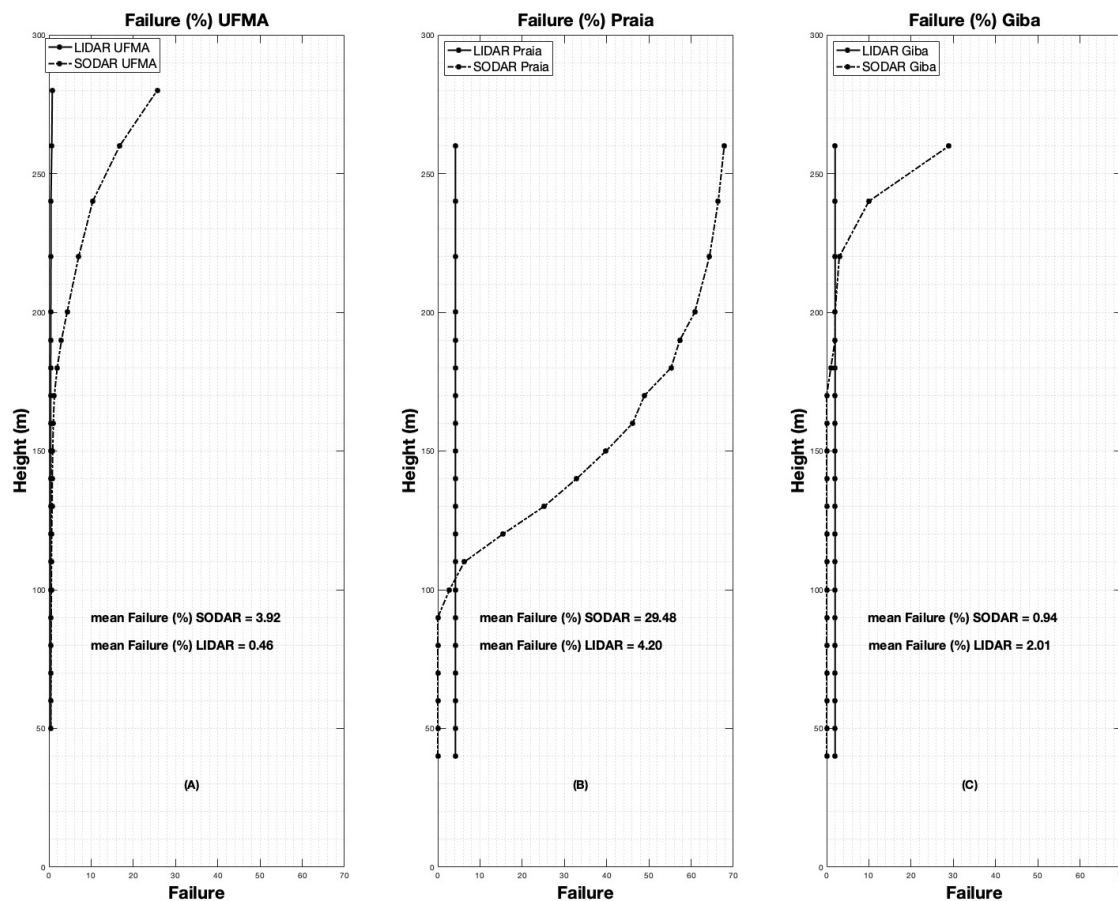


Figure 8. LIDAR and SODAR performance (% failure) based on height for all three campaigns: *UFMA* (A), *Praia* (B), and *Giba* (C). Note that LIDAR was 3.5 m from the surface in the *UFMA* campaign.

A decrease in SODAR performance has been reported in other studies. [79] (2021) analyzed about 7 years of data (from 2008 to 2016) at the Ahtopol Meteorological Observatory, about 400 m away from the Black Sea (Bulgaria) at latitude $42^{\circ}5'2.03''$ N. The records were taken every 10 min and filtered by a moving average of 20 min between 30 m and 600 m in height, with a 10-m resolution above 150 m. The equipment was also a SODAR Sintec MFAS with frequencies in the range of 1650–2750 Hz and multi-beam operation of nine emission and reception angles (0° , $\pm 9.3^{\circ}$, $\pm 15.6^{\circ}$, $\pm 22.1^{\circ}$, and $\pm 29^{\circ}$). The average efficiency data declined above 120 m (10% failure) and reached 20% failure at about 240 m, decreasing to 50% at 250 m.

Even considering the significant difference in latitude and hemisphere, we had considerable similarities in the performance of our SODAR compared to that of [79] (2021), mainly in the place closest to the beach (*Praia* in Figure 8).

The average vertical profiles of the horizontal wind speed were calculated by $|V| = \sqrt{u^2 + v^2}$, where u is the zonal component and v is the meridional component. In

the *UFMA* campaign, the profiles show the speeds sampled by LIDAR as being slightly higher than those of SODAR from 50 m to about 140 m, and from there, an inversion occurred, with the intensities sampled by SODAR being higher than those of LIDAR (*UFMA* in Figure 9).

In the coastal region (*Praia* campaign), the mean wind speed sampled by SODAR was lower at heights greater than 120 m (Figure 9), which is explained by the decreased performance of this equipment, which had data failures during this campaign, as shown in Figure 8.

These failures can also be observed in Figure 10 when we examine the wind speed plot as a function of height and time. When the wind direction was coming from the ocean, the SODAR signal-to-noise ratio decreased (northeast direction). In this case, the flow suffered less influence from surface roughness effects generating fewer inhomogeneities in the air density field, which were the SODAR targets.

Still observing Figure 10, we found that a wind speed greater than 10 ms^{-1} remained until approximately 5:30 a.m. From this moment, the wind speed abruptly dropped to values below 2 ms^{-1} , and the wind direction changed, coming from the continent (southeast direction). Thus, the SODAR started to record values at heights above 120 m.

For the data sampled in the *Giba* campaign, the intensity behavior was more homogeneous and more similar to the *UFMA* campaign data (*Giba* in Figure 9).

The PCCs, as a function of height, are plotted in Figure 11 for the different campaigns. The curves are separated into zonal in Figure 11A, meridional in Figure 11B, and vertical components in Figure 11C. The zonal and meridional components shows higher PCC values (Figure 11A,B), whereas the vertical component shows somewhat lower values (Figure 11C). The curves generated with the data obtained at *Praia* are slightly different from the others due to the loss of information from the SODAR at the beginning of the sample period (Figure 10).

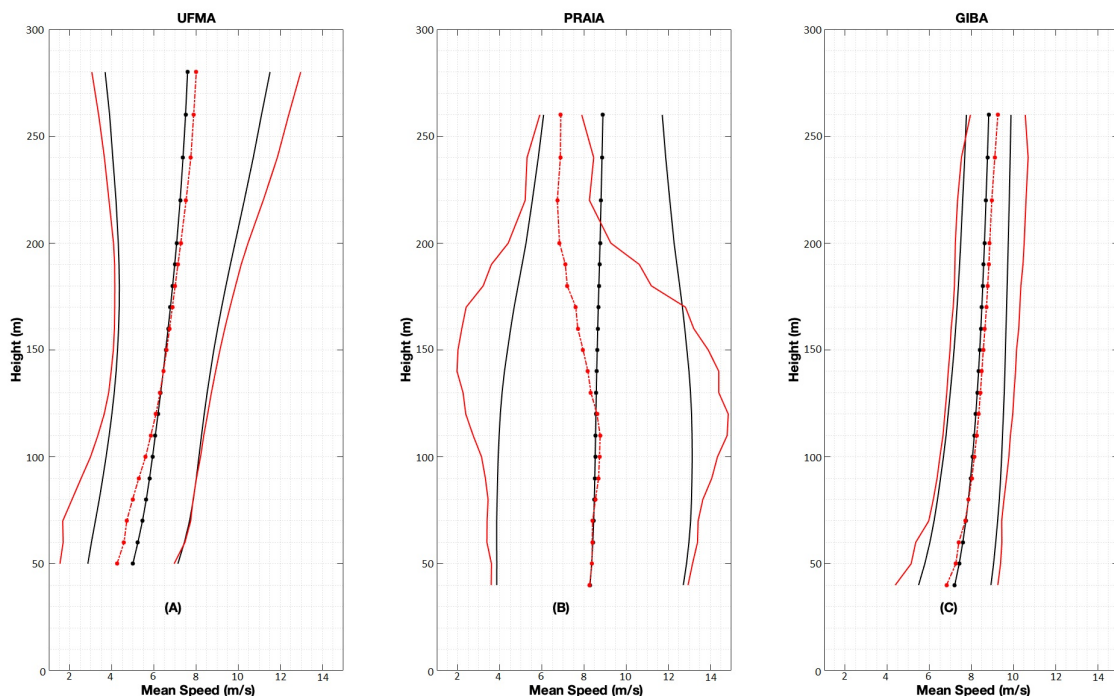


Figure 9. Mean wind speed profiles of LIDAR (black dotted lines) and SODAR (red dotted lines) obtained in the three campaigns: *UFMA* (A), *Praia* (B), and *Giba* (C). The lines represent the variance in the average speed, with LIDAR in black and SODAR in red. Note that the LIDAR was 3.5 m from the surface in the *UFMA* campaign.

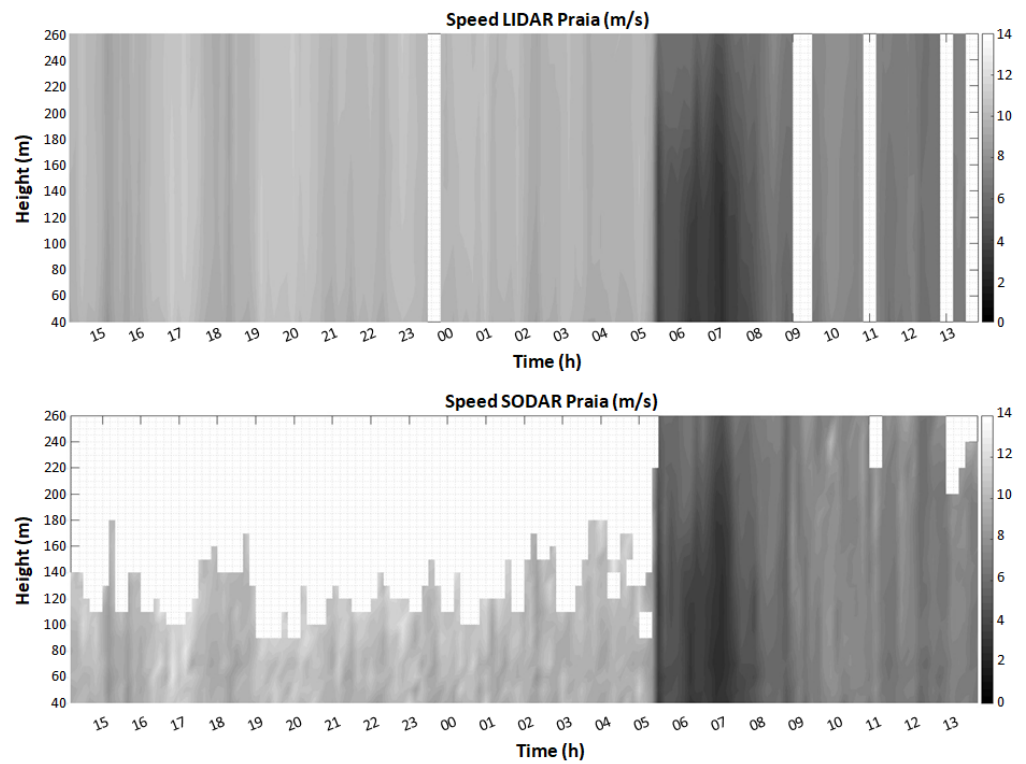


Figure 10. Wind speed as a function of time and height for the *Praia* campaign, estimated by LIDAR and SODAR.

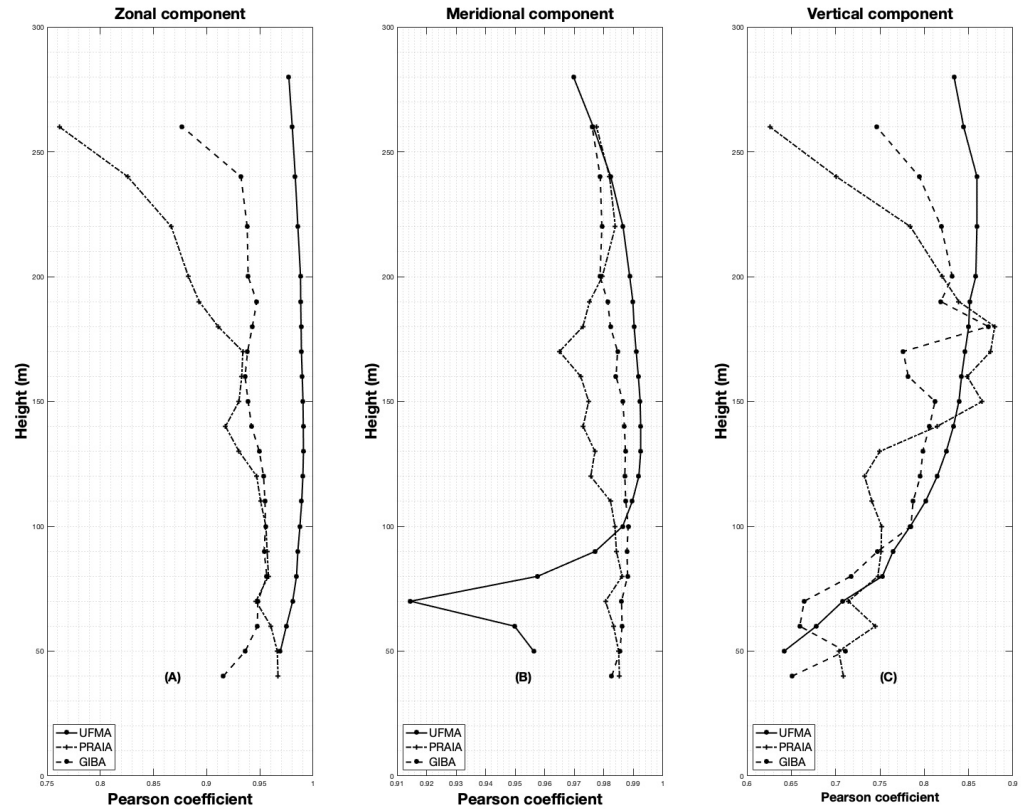


Figure 11. Pearson’s correlation coefficients (PCCs) between LIDAR and SODAR for the three campaigns: *UFMA*, *Praia*, and *Giba*. The panels refer to the correlation of the zonal (east-west) (A), meridional (north-south) (B), and vertical (C) components of the wind speed vector. Note that the LIDAR was 3.5 m from the surface in the *UFMA* campaign.

Table 3 presents the spatial means of the Pearson's correlation coefficients (MPCCs) while also considering all vertical levels. In general, the coefficients of the horizontal components were higher than those of the vertical components. The results also indicate higher average coefficients for the *UFMA* campaign (MPCC = 0.93), followed by *Giba* (MPCC = 0.99) and *Praia* (MPCC = 0.89).

In Table 4, the MPCCs are presented for the average between the vertical levels from 50 to 150 m, with similar performance for the *Praia* and *Giba* campaigns (MPCC = 0.89).

In Table 5, the MPCCs are presented for the average between the vertical levels from 150 to 260 m. The results illustrate a lower MPCC in the *Praia* campaign for all velocity components. The incremental loss of data quality with height in *Praia* led to a decrease in the PCC in this height interval.

It is noted in Tables 3–5 that the correlations of the vertical component were smaller compared with those of the horizontal ones. This was due to the distance between the equipment and the non-overlap of the sampled layer in the vertical measurement.

Table 3. Means of Pearson's correlation coefficients (MPCCs) of the zonal, meridional, and vertical wind speed components during the three campaigns—*UFMA*, *Praia*, and *Giba*—for all vertical levels.

	UFMA	Praia	Giba	Mean
Zonal	0.99	0.92	0.94	0.95
Meridional	0.98	0.98	0.98	0.98
Vertical	0.81	0.77	0.77	0.78
Mean	0.93	0.89	0.90	

Table 4. Means of Pearson's correlation coefficients (MPCCs) of the zonal, meridional, and vertical wind speed components during the three campaigns—*UFMA*, *Praia*, and *Giba*—for vertical levels from 50 to 150 m.

	UFMA	Praia	Giba	Mean
Zonal	0.98	0.95	0.95	0.96
Meridional	0.97	0.98	0.99	0.98
Vertical	0.77	0.74	0.74	0.75
Mean	0.91	0.89	0.89	

Table 5. Means of Pearson's correlation coefficients (MPCCs) of the zonal, meridional, and vertical wind speed components during the three campaigns—*UFMA*, *Praia*, and *Giba*—for vertical levels from 150 to 260 m.

	UFMA	Praia	Giba	Mean
Zonal	0.99	0.88	0.93	0.93
Meridional	0.99	0.98	0.98	0.98
Vertical	0.85	0.80	0.81	0.82
Mean	0.94	0.89	0.91	

7. Summary and Conclusions

In this paper, we had the opportunity to compare two remote sensors to quantify how their estimated parameters agreed or diverged. In addition to this comparison, it was possible to observe the conditions that interfered with the sampling efficiency (i.e., how much each device utilized the collected information). The behavior of the vertical distribution of the mean velocity in the first 100 m showed lower speeds during the *UFMA* campaign due to this campaign being carried out in an urban region, unlike the locations of the *Praia* and *Giba* campaigns.

LIDAR performed better concerning the loss of sampling efficiency compared with SODAR over the three campaigns. While the first lost about 1%, 4%, and 2% in the campaigns of *UFMA*, *Praia*, and *Giba*, respectively, the second one lost more efficiency at heights above

100 m. In the *UFMA* and *Giba* campaigns, SODAR lost efficiency from approximately 10 to 30% above 170 m and lost between 65 and 75% above 100 m in the *Praia* campaign.

Regarding the average vertical profile of the horizontal velocity, both sensors performed similarly in the *UFMA* and *Giba* campaigns, with SODAR showing higher values above 150 m and 90 m, respectively. In the *Praia* campaign, above 120 m, it was observed that these values were discrepant, which is explained by the lack of information collected by SODAR, as it only started to record values again after the decrease in the mean speed ($<2 \text{ ms}^{-1}$), as shown in Figure 10.

The correlations between the remote sensors for the zonal, meridional, and vertical components obtained using LIDAR and SODAR during the *UFMA*, *Praia*, and *Giba* campaigns are listed in Tables 3–5. In general, the coefficients of the horizontal components were higher, presenting values greater than 0.9 in all campaigns, while the vertical component obtained values between 0.7 and 0.85.

For the coastal region of Maranhão, by observing the differences between the sensors, and despite the flaws presented, it is concluded that LIDAR and SODAR can be used in the evaluation of meteorological parameters to estimate the wind potential mainly for the conversion of electric energy by wind turbines.

Author Contributions: Conceptualization, A.R.T.J., N.P.S., A.T.A., F.L.A.N., F.M.P., R.M.d.F., O.R.S., C.B.M.O., D.C.P.L., S.L.d.L., R.B.S.V. and D.Q.O.; methodology, A.R.T.J., N.P.S., A.T.A., F.L.A.N., F.M.P., R.M.d.F., O.R.S., C.B.M.O., D.C.P.L., S.L.d.L., R.B.S.V. and D.Q.O.; software, A.R.T.J., N.P.S., D.C.P.L., R.B.S.V. and D.Q.O.; formal analysis, A.R.T.J., N.P.S., A.T.A., F.L.A.N., F.M.P., R.M.d.F. and O.R.S.; investigation, A.R.T.J. and N.P.S.; data curation, A.R.T.J. and N.P.S.; writing—original draft preparation, A.R.T.J., N.P.S., A.T.A., F.L.A.N., F.M.P., R.M.d.F., O.R.S., C.B.M.O., D.C.P.L., S.L.d.L., R.B.S.V. and D.Q.O.; writing—review and editing, A.R.T.J., N.P.S., A.T.A., F.L.A.N., F.M.P., R.M.d.F., O.R.S., C.B.M.O., D.C.P.L., S.L.d.L., R.B.S.V. and D.Q.O.; supervision, D.Q.O. and O.R.S.; project administration, D.Q.O.; funding acquisition, D.Q.O. and O.R.S. All authors have read and agreed to the published version of the manuscript.

Funding: The authors acknowledge funding from Equatorial Energia and Gera Maranhão under the Brazilian Electricity Regulatory Agency's (ANEEL) R&D Program (PD-00037-0042/2020), the National Council for Scientific and Technological Development of Brazil (CNPq), the Foundation for Support to Research and Scientific and Technological Development of Maranhão (FAPEMA), Coordination for the Improvement of Higher Education Personnel (CAPES), and the National Institute of Science & Technology in Ocean and Fluvial Energies (INEOF).

Institutional Review Board Statement: Not applicable.

Informed Consent Statement: Not applicable.

Data Availability Statement: Not applicable.

Acknowledgments: This study was supported by the Brazilian Electricity Regulatory Agency (ANEEL) under an R&D project (PD-00037-0042/2020) funded by Gera Maranhão S.A. and Equatorial Energia S.A. The authors also acknowledge support from the National Council for Scientific and Technological Development of Brazil (CNPq), the Foundation for Support to Research and Scientific and Technological Development of Maranhão (FAPEMA), Coordination for the Improvement of Higher Education Personnel (CAPES), and the National Institute of Science & Technology in Ocean and Fluvial Energies (INEOF). We are thankful to Gilberto Porto and Dalila Porto for their continuous support and cooperation.

Conflicts of Interest: The authors declare no conflict of interest.

References

1. Assireu, A.T.; Pimenta, F.M.; de Freitas, R.M.; Saavedra, O.R.; Neto, F.L.A.; Torres, A.R., Jr.; Oliveira, C.B.M.; Lopes, D.C.P.; de Lima, S.L.; Veras, R.B.S.; et al. EOSOLAR Project: Assessment of wind resources of a coastal equatorial region of Brazil—Overview and preliminary results. *Energies* **2022**, *15*, 2319. [[CrossRef](#)]
2. Stickland, M.; Scanlon, T.; Fabre, S. Comparison of Zephir and Windcube measurements in the same complex flowfield. In Proceedings of the EWEA OFFSHORE 2011, Amsterdam, The Netherlands, 29 November–1 December 2011; University of Strathclyde: Glasgow, UK, 2011.

3. Lang, S.; McKeogh, E. LIDAR and SODAR measurements of wind speed and direction in upland terrain for wind energy purposes. *Remote Sens.* **2011**, *3*, 1871–1901. [[CrossRef](#)]
4. Antoniou, I.; Jørgensen, H.E.; Ormel, F.; Bradley, S.; von Hünerbein, S.; Emeis, S.; Warmbier, G. *On the Theory of SODAR Measurement Techniques*; OCLC: 473721156; Risø National Laboratory, Information Service Department: Roskilde, Denmark, 2003.
5. Kallistratova, M.A.; Petenko, I.V.; Kouznetsov, R.D.; Kulichkov, S.N.; Chkhetiani, O.G.; Chunchusov, I.P.; Lyulyukin, V.S.; Zaitseva, D.V.; Vazaeva, N.V.; Kuznetsov, D.D.; et al. Sodar sounding of the atmospheric boundary layer: Review of studies at the Obukhov Institute of Atmospheric Physics, Russian Academy of Sciences. *Izv. Atmos. Ocean. Phys.* **2018**, *54*, 242–256. [[CrossRef](#)]
6. Kelley, N.D.; Jonkman, B.J.; Scott, G.N.; Pichugina, Y.L. *Comparing Pulsed Doppler LIDAR with SODAR and Direct Measurements for Wind Assessment*; Technical Report; National Renewable Energy Lab. (NREL): Golden, CO, USA, 2007.
7. Sotelino, L.G.; Coster, N.D.; Beirinckx, P.; Peeters, P. Intercomparison of Cup Anemometer and Sonic Snemometers on Site at Uccle/Belgium. In Proceedings of the WMO Technical Conference on Meteorological and Environmental Instruments and Methods of Observation (TECO-2012), Brussels, Belgium, 16–18 October 2012; p. 7.
8. Dubov, D.; Aprahamian, B.; Aprahamian, M. Comparison between conventional wind measurement systems and SODAR systems for remote sensing including examination of real wind data. In Proceedings of the 2017 15th International Conference on Electrical Machines, Drives and Power Systems (ELMA), Sofia, Bulgaria, 1–3 June 2017; IEEE: Piscataway, NJ, USA 2017; pp. 106–109. [[CrossRef](#)]
9. Finn, A.; Rogers, K.; Rice, F.; Meade, J.; Holland, G.; May, P. A comparison of vertical atmospheric wind profiles obtained from monostatic Sodar and unmanned aerial vehicle-based acoustic tomography. *J. Atmos. Ocean. Technol.* **2017**, *34*, 2311–2328. [[CrossRef](#)]
10. Sinha, S.; Regeena, M.L.; Sarma, T.V.C.; Hashiguchi, H.; Tuckley, K.R. Doppler Profile Tracing Using MPCF on MU Radar and Sodar: Performance Analysis. *IEEE Geosci. Remote Sens. Lett.* **2018**, *15*, 508–511. [[CrossRef](#)]
11. Buzdugan, L.; Stefan, S. A comparative study of SODAR, LIDAR wind measurements and aircraft derived wind observations. *Rom. J. Phys.* **2020**, *65*, 810.
12. Buzdugan, L.; Bugeac, O.P.; Stefan, S. A comparison of low-level wind profiles from Mode-S EHS data with ground-based remote sensing data. *Meteorol. Atmos. Phys.* **2021**, *133*, 1455–1468. [[CrossRef](#)]
13. Zhou, Z.; Bu, Z. Wind measurement comparison of Doppler lidar with wind cup and L band sounding radar. *Atmos. Meas. Tech. Discuss.* **2021**, preprint. [[CrossRef](#)]
14. Aitken, M.L.; Rhodes, M.E.; Lundquist, J.K. Performance of a Wind-Profiling Lidar in the Region of Wind Turbine Rotor Disks. *J. Atmos. Ocean. Technol.* **2012**, *29*, 347–355. [[CrossRef](#)]
15. Kumer, V.M.; Reuder, J.; Furevik, B.R. A Comparison of LiDAR and Radiosonde Wind Measurements. *Energy Procedia* **2014**, *53*, 214–220. [[CrossRef](#)]
16. Alfredini, P.; Arasaki, E.; Fortner, E. Behavior of sea level in the period of 1980 to 2017 on the port area of Gulf of Maranhão, Brazil. *Transnav Int. J. Mar. Navig. Saf. Sea Transp.* **2021**, *15*, 683–686. [[CrossRef](#)]
17. Philander, S.G.H. El Niño Southern Oscillation phenomena. *Nature* **1983**, *302*, 295–301. [[CrossRef](#)]
18. Philander, S.; Seigel, A. Chapter 33 Simulation of El Niño of 1982–1983. In *Deep Sea Research Part II: Topical Studies in Oceanography*; Elsevier: Amsterdam, The Netherlands, 1985; Volume 40, pp. 517–541. [[CrossRef](#)]
19. Philander, S.G.; Rasmusson, E.M. The Southern Oscillation and El Niño. In *Advances in Geophysics*; Elsevier: Amsterdam, The Netherlands, 1985; Volume 28, pp. 197–215. [[CrossRef](#)]
20. Philander, G. El Niño and La Niña. *Am. Sci.* **1989**, *77*, 451–459.
21. Kane, R.P. Prediction of Droughts in North-East Brazil: Role of ENSO and Use of Periodicities. *Int. J. Climatol.* **1997**, *17*, 655–665. [[CrossRef](#)]
22. Goddard, L.; Philander, S.G. The Energetics of El Niño and La Niña. *J. Clim.* **2000**, *13*, 1496–1516. [[CrossRef](#)]
23. Grimm, A.M. The El Niño Impact on the Summer Monsoon in Brazil: Regional Processes versus Remote Influences. *J. Clim.* **2003**, *16*, 263–280. [[CrossRef](#)]
24. Philander, S.G.; Fedorov, A. Is El Niño Sporadic or Cyclic? *Annu. Rev. Earth Planet. Sci.* **2003**, *31*, 579–594. [[CrossRef](#)]
25. Hastenrath, S. Circulation and teleconnection mechanisms of Northeast Brazil droughts. *Prog. Oceanogr.* **2006**, *70*, 407–415. [[CrossRef](#)]
26. Philander, S.G. *Our Affair with El Niño: How We Transformed an Enchanting Peruvian Current Into a Global Climate Hazard*; Princeton University Press: Princeton, NJ, USA, 2006.
27. Kayano, M.T.; Andreoli, R.V. Relationships between rainfall anomalies over northeastern Brazil and the El Niño–Southern Oscillation. *J. Geophys. Res.* **2006**, *111*, D13101. [[CrossRef](#)]
28. Rodrigues, R.R.; Haarsma, R.J.; Campos, E.J.D.; Ambrizzi, T. The Impacts of Inter–El Niño Variability on the Tropical Atlantic and Northeast Brazil Climate. *J. Clim.* **2011**, *24*, 3402–3422. [[CrossRef](#)]
29. Cai, W.; McPhaden, M.J.; Grimm, A.M.; Rodrigues, R.R.; Taschetto, A.S.; Garreaud, R.D.; Dewitte, B.; Poveda, G.; Ham, Y.G.; Santoso, A.; et al. Climate impacts of the El Niño–Southern Oscillation on South America. *Nat. Rev. Earth Environ.* **2020**, *1*, 215–231. [[CrossRef](#)]
30. Costa, M.d.S.; Oliveira-Júnior, J.F.d.; Santos, P.J.d.; Correia Filho, W.L.F.; Gois, G.d.; Blanco, C.J.C.; Teodoro, P.E.; Silva Junior, C.A.d.; Santiago, D.d.B.; Souza, E.d.O.; et al. Rainfall extremes and drought in Northeast Brazil and its relationship with El Niño–Southern Oscillation. *Int. J. Climatol.* **2021**, *41*, 6835. [[CrossRef](#)]

31. Glenn, A.H. Circulation and Convergence in the Equatorial Zone Between 95° E and 160° E: December to February*. *Bull. Am. Meteorol. Soc.* **1947**, *28*, 453–464. [\[CrossRef\]](#)
32. Simpson, R.H. Synoptic Aspects of the Intertropical Convergence Near Central and South America. *Bull. Am. Meteorol. Soc.* **1947**, *28*, 335–346. [\[CrossRef\]](#)
33. Miles, M.K. Meteorology. *Sci. Prog. (1933)* **1948**, *36*, 86–101.
34. Crowe, P.R. The seasonal variation in the strength of the trades. In *Transactions and Papers (Institute of British Geographers)*; Wiley: Hoboken, NJ, USA, 1950; p. 25. [\[CrossRef\]](#)
35. Waliser, D.E.; Somerville, R.C.J. Preferred latitudes of the Intertropical Convergence Zone. *J. Atmos. Sci.* **1994**, *51*, 1619–1639. [\[CrossRef\]](#)
36. Philander, S.G.H.; Gu, D.; Lambert, G.; Li, T.; Halpern, D.; Lau, N.C.; Pacanowski, R.C. Why the ITCZ Is Mostly North of the Equator. *J. Clim.* **1996**, *9*, 2958–2972. [\[CrossRef\]](#)
37. Gomes, H.B.; Ambrizzi, T.; Herdies, D.L.; Hodges, K.; Pontes da Silva, B.F. Easterly Wave Disturbances over Northeast Brazil: An Observational Analysis. *Adv. Meteorol.* **2015**, *2015*, 176238. [\[CrossRef\]](#)
38. Waliser, D.; Jiang, X. Tropical meteorology and climate: Intertropical Convergence Zone. In *Encyclopedia of Atmospheric Sciences*; Elsevier: Amsterdam, The Netherlands, 2015; pp. 121–131. [\[CrossRef\]](#)
39. Nogués-Paegle, J.; Mechoso, C.R.; Fu, R.; Berbery, E.H.; Chao, W.C.; Chen, T.C.; Cook, K.; Diaz, A.F.; Enfield, D.; Ferreira, R.; et al. Progress in Pan American CLIVAR research: Understanding the South American monsoon. *Meteorologica* **2002**, *27*, 1–30.
40. Gan, M.A.; Kousky, V.E.; Ropelewski, C.F. The South America Monsoon Circulation and Its Relationship to Rainfall over West-Central Brazil. *J. Clim.* **2004**, *17*, 47–66. [\[CrossRef\]](#)
41. Liebmann, B.; Mechoso, C.R. The South American Monsoon System. In *World Scientific Series on Asia-Pacific Weather and Climate*, 2nd ed.; World Scientific: Singapore, 2011; Volume 5, pp. 137–157. [\[CrossRef\]](#)
42. Marengo, J.A.; Liebmann, B.; Grimm, A.M.; Misra, V.; Silva Dias, P.L.; Cavalcanti, I.F.A.; Carvalho, L.M.V.; Berbery, E.H.; Ambrizzi, T.; Vera, C.S.; et al. Recent developments on the South American monsoon system: Recent Developments on the South American Monsoon System. *Int. J. Climatol.* **2012**, *32*, 1–21. [\[CrossRef\]](#)
43. Vuille, M.; Burns, S.J.; Taylor, B.L.; Cruz, F.W.; Bird, B.W.; Abbott, M.B.; Kanner, L.C.; Cheng, H.; Novello, V.F. A review of the South American monsoon history as recorded in stable isotopic proxies over the past two millennia. *Clim. Past* **2012**, *8*, 1309–1321. [\[CrossRef\]](#)
44. de Carvalho, L.M.V.; Cavalcanti, I.F.A. The South American Monsoon System (SAMS). In *The Monsoons and Climate Change*; de Carvalho, L.M.V., Jones, C., Eds.; Springer Climate; Springer International Publishing: Cham, Switzerland, 2016; pp. 121–148. [\[CrossRef\]](#)
45. Correa, I.C.; Arias, P.A.; Rojas, M. Evaluation of multiple indices of the South American monsoon. *Int. J. Climatol.* **2021**, *41*, E2801–E2819. [\[CrossRef\]](#)
46. Madden, R.A.; Julian, P.R. Detection of a 40–50 Day Oscillation in the Zonal Wind in the Tropical Pacific. *J. Atmos. Sci.* **1971**, *28*, 702–708. [\[CrossRef\]](#)
47. Madden, R.A.; Julian, P.R. Description of Global-Scale Circulation Cells in the Tropics with a 40–50 Day Period. *J. Atmos. Sci.* **1972**, *29*, 1109–1123. [\[CrossRef\]](#)
48. Madden, R.A.; Julian, P.R. Observations of the 40–50-Day Tropical Oscillation—A Review. *Mon. Weather. Rev.* **1994**, *122*, 814–837. [\[CrossRef\]](#)
49. de Souza, E.B.; Ambrizzi, T. Modulation of the intraseasonal rainfall over tropical Brazil by the Madden–Julian oscillation. *Int. J. Climatol.* **2006**, *26*, 1759–1776. [\[CrossRef\]](#)
50. Alvarez, M.S.; Vera, C.S.; Kiladis, G.N.; Liebmann, B. Influence of the Madden Julian Oscillation on precipitation and surface air temperature in South America. *Clim. Dyn.* **2016**, *46*, 245–262. [\[CrossRef\]](#)
51. Mayta, V.C.; Ambrizzi, T.; Espinoza, J.C.; Silva Dias, P.L. The role of the Madden-Julian oscillation on the Amazon Basin intraseasonal rainfall variability. *Int. J. Climatol.* **2019**, *39*, 343–360. [\[CrossRef\]](#)
52. Mayta, V.C.; Silva, N.P.; Ambrizzi, T.; Dias, P.L.S.; Espinoza, J.C. Assessing the skill of all-season diverse Madden–Julian oscillation indices for the intraseasonal Amazon precipitation. *Clim. Dyn.* **2020**, *54*, 3729–3749. [\[CrossRef\]](#)
53. Zhang, C.; Adames, A.F.; Khouider, B.; Wang, B.; Yang, D. Four theories of the Madden-Julian Oscillation. *Rev. Geophys.* **2020**, *58*, e2019RG000685. [\[CrossRef\]](#)
54. Vasconcelos Junior, F.d.C.; Jones, C.; Gandu, A.W.; Martins, E.S.P.R. Impacts of the Madden-Julian Oscillation on the intensity and spatial extent of heavy precipitation events in northern Northeast Brazil. *Int. J. Climatol.* **2021**, *41*, 3628–3639. [\[CrossRef\]](#)
55. Sena, A.C.T.; Peings, Y.; Magnusdottir, G. Effect of the Quasi-Biennial Oscillation on the Madden Julian Oscillation Teleconnections in the Southern Hemisphere. *Geophys. Res. Lett.* **2022**, *49*, e2021GL096105. [\[CrossRef\]](#)
56. Serra, Y.L.; Kiladis, G.N.; Cronin, M.F. Horizontal and Vertical Structure of Easterly Waves in the Pacific ITCZ. *J. Atmos. Sci.* **2008**, *65*, 1266–1284. [\[CrossRef\]](#)
57. Toma, V.E.; Webster, P.J. Oscillations of the Intertropical Convergence Zone and the genesis of easterly waves. Part I: Diagnostics and theory. *Clim. Dyn.* **2010**, *34*, 587–604. [\[CrossRef\]](#)
58. Toma, V.E.; Webster, P.J. Oscillations of the Intertropical Convergence Zone and the genesis of easterly waves Part II: Numerical verification. *Clim. Dyn.* **2010**, *34*, 605–613. [\[CrossRef\]](#)

59. Xie, S.P.; Carton, J.A. Tropical atlantic variability: Patterns, mechanisms, and impacts. In *Geophysical Monograph Series*; Wang, C., Xie, S., Carton, J., Eds.; American Geophysical Union: Washington, DC, USA, 2013; pp. 121–142. [[CrossRef](#)]
60. Gomes, H.B.; Ambrizzi, T.; Pontes da Silva, B.F.; Hodges, K.; Silva Dias, P.L.; Herdies, D.L.; Silva, M.C.L.; Gomes, H.B. Climatology of easterly wave disturbances over the tropical South Atlantic. *Clim. Dyn.* **2019**, *53*, 1393–1411. [[CrossRef](#)]
61. de Medeiros, F.J.; de Oliveira, C.P.; Torres, R.R. Climatic aspects and vertical structure circulation associated with the severe drought in Northeast Brazil (2012–2016). *Clim. Dyn.* **2020**, *55*, 2327–2341. [[CrossRef](#)]
62. Roxburgh, W. XLVII. On the land winds of Coromandel, and their causes. *The Philosophical Magazine*, 1 October 1810; Volume 36, pp. 243–253. [[CrossRef](#)]
63. Hall, F. XXIII. Meteorological observations made during a residence in Colombia between the years 1820 and 1830. *London Edinburgh Dublin Philos. Mag. J. Sci.* **1838**, *12*, 148–158. [[CrossRef](#)]
64. Hopkins, T. LXVIII. On the diurnal change of the aqueous portion of the atmosphere, and their effects on the barometer. *London Edinburgh Dublin Philos. Mag. J. Sci.* **1845**, *27*, 427–435. [[CrossRef](#)]
65. Sabine. VIII. On some points in the meteorology of Bombay. *London Edinburgh Dublin Philos. Mag. J. Sci.* **1846**, *28*, 24–35. [[CrossRef](#)]
66. Kousky, V.E. Diurnal rainfall variation in northeast Brazil. *Mon. Weather. Rev.* **1980**, *108*, 488–498. [[CrossRef](#)]
67. Planchon, O.; Damato, F.; Dubreuil, V.; Gouery, P. A method of identifying and locating sea-breeze fronts in north-eastern Brazil by remote sensing. *Meteorol. Appl.* **2006**, *13*, 225. [[CrossRef](#)]
68. Souza, D.C.d.; Oyama, M.D. Breeze potential along the brazilian northern and northeastern coast. *J. Aerosp. Technol. Manag.* **2017**, *9*, 368–378. [[CrossRef](#)]
69. Ribeiro, F.N.; Oliveira, A.P.d.; Soares, J.; Miranda, R.M.d.; Barlage, M.; Chen, F. Effect of sea breeze propagation on the urban boundary layer of the metropolitan region of Sao Paulo, Brazil. *Atmos. Res.* **2018**, *214*, 174–188. [[CrossRef](#)]
70. Anjos, M.; Lopes, A. Sea breeze front identification on the northeastern coast of Brazil and its implications for meteorological conditions in the Sergipe region. *Theor. Appl. Climatol.* **2019**, *137*, 2151–2165. [[CrossRef](#)]
71. Anjos, M.; Lopes, A.; Lucena, A.J.d.; Mendonça, F. Sea breeze front and outdoor thermal comfort during summer in northeastern Brazil. *Atmosphere* **2020**, *11*, 1013. [[CrossRef](#)]
72. Wang, L.; Qiang, W.; Xia, H.; Wei, T.; Yuan, J.; Jiang, P. Robust solution for boundary layer height detections with coherent doppler wind lidar. *Adv. Atmos. Sci.* **2021**, *38*, 1920–1928. [[CrossRef](#)]
73. LEOSPHERE. *Windcube FCR Measurements*; LEOSPHERE: Saclay, France, 2017.
74. ScintecAG. *Scintec Flat Array Sodars—Theory Manual (SFAS, MFAS, XFAS) Including RASS RAE1 and WindRASS*, Version 1.03 ed.; Technical Report; ScintecAG: Princeton, NJ, USA, 2017.
75. Kelberlau, F.; Mann, J. Cross-contamination effect on turbulence spectra from Doppler beam swinging wind lidar. *Wind. Energy Sci.* **2020**, *5*, 519–541. [[CrossRef](#)]
76. Chatfield, C. *The Analysis of Time Series: An Introduction*, 6th ed.; OCLC: 880737910; Taylor and Francis: Hoboken, NJ, USA 2013.
77. Bertrand, C.; González Sotelino, L.; Journée, M. Quality control of the RMI's AWS wind observations. *Adv. Sci. Res.* **2016**, *13*, 13–19. [[CrossRef](#)]
78. Lo Feudo, T.; Calidonna, C.R.; Avolio, E.; Sempreviva, A.M. Study of the vertical structure of the coastal boundary layer integrating surface measurements and ground-based remote sensing. *Sensors* **2020**, *20*, 6516. [[CrossRef](#)] [[PubMed](#)]
79. Barantiev, D.; Batchvarova, E. Wind speed profile statistics from acoustic soundings at a black sea coastal site. *Atmosphere* **2021**, *12*, 1122. [[CrossRef](#)]